

Feature selection for classification of blazars based on optical photometric and polarimetric time-series data

Makoto UEMURA,^{1,*} Taisei ABE,¹ Yurika YAMADA,¹ and Shiro IKEDA ²

¹Hiroshima Astrophysical Science Center, Hiroshima University, 1-3-1 Kagamiyama, Higashi-Hiroshima, Hiroshima 739-8526, Japan

²The Institute of Statistical Mathematics, 10-3 Midori-cho, Tachikawa, Tokyo 190-8562, Japan

*E-mail: uemuram@hiroshima-u.ac.jp

Received 2020 March 19; Accepted 2020 June 14

Abstract

Blazars can be divided into two subtypes, flat spectrum radio quasars (FSRQs) and BL Lac objects, which have been distinguished phenomenologically by the strength of their optical emission lines, while their physical nature and relationship are still not fully understood. We focus on the differences in their variability. We characterize the blazar variability using the Ornstein–Uhlenbeck (OU) process, and investigate the features that are discriminative for the two subtypes. We used optical photometric and polarimetric data obtained with the 1.5 m Kanata telescope for 2008–2014. We found that four features, namely the variation amplitude, characteristic timescale, and non-stationarity of the variability obtained from the light curves and the median of the degree of polarization (PD), are essential for distinguishing between FSRQs and BL Lac objects. FSRQs are characterized by rare and large flares, while the variability of BL Lac objects can be reproduced with a stationary OU process with relatively small amplitudes. The characteristics of the variability are governed not by the differences in the jet structure between the subtypes, but by the peak frequency of the synchrotron emission. This implies that the nature of the variation in the jets is common in FSRQs and BL Lac objects. We found that BL Lac objects tend to have high PD medians, which suggests that they have a stable polarization component. FSRQs have no such component, possibly because of a strong Compton cooling effect in sub-parsec-scale jets.

Key words: BL Lacertae objects: general — galaxies: active — galaxies: statistics

1 Introduction

Blazars are a subclass of active galactic nuclei (AGN) with relativistic jets that point toward us. The jet emission is amplified by the beaming effect and dominates the observed flux at almost all wavelengths (Blandford & Rees 1978; Blandford & Königl 1979; Urry & Padovani 1995). Synchrotron emission from the jet is dominant in the radio–X-ray regime. The observed X-ray– γ -ray emission

is mostly due to inverse Compton scattering by relativistic electrons in the jet. Blazars exhibit violent variability, which provides a hint for understanding the physical conditions and structure in AGN jets (e.g., Ulrich et al. 1997).

Blazars consist of two subtypes: flat spectrum radio quasars (FSRQs) and BL Lac type objects. The former was originally defined by strong emission lines observed in the optical spectra (equivalent width $> 5 \text{ \AA}$; Stickel et al.

1991; Stocke et al. 1991), while the latter was defined by weaker lines or featureless spectra. In addition, FSRQs have lower peak frequencies in the synchrotron emission, $\nu_{\text{peak}} \lesssim 10^{14}$ Hz, in their spectral energy distribution (SED), while BL Lac objects have a wide range of ν_{peak} ($10^{14} \lesssim \nu_{\text{peak}}$ [Hz] $\lesssim 10^{18}$; Abdo et al. 2010). The luminosity of blazars has a negative correlation with ν_{peak} ; FSRQs form the most luminous class of blazars, while BL Lac objects are less luminous. In SEDs, the relative strength of the inverse Compton scattering component to the synchrotron component is larger in FSRQs than in BL Lac objects. These regularities are known as the “blazar sequence” (Ghisellini et al. 1998).

In addition to classification based on the emission line strength, a classification scheme based on ν_{peak} is also used for blazars, with low synchrotron peaked (LSP) blazars for objects with $\nu_{\text{peak}} \lesssim 10^{14}$ Hz, intermediate synchrotron peaked (ISP) blazars with $10^{14} \lesssim \nu_{\text{peak}}$ [Hz] $\lesssim 10^{15}$, and high synchrotron peaked (HSP) blazars with $\nu_{\text{peak}} \gtrsim 10^{15}$ Hz (Abdo et al. 2010). Most FSRQs are LSP blazars. In this paper, we call LSP, ISP, and HSP BL Lac objects LBLs, IBLs, and HBLs, respectively.

The nature of and links between blazar subtypes are still incompletely understood. Ghisellini and Tavecchio (2008) proposed that FSRQs are AGN having a radiatively efficient accretion disk (a “standard” disk; Shakura & Sunyaev 1973) with a high accretion rate, while BL Lac objects have a radiatively inefficient accretion flow (RIAF; Narayan & Yi 1995; Quataert 2001) with a low accretion rate. The accretion rate is considered to be linked to the extended radio morphology of radio galaxies, that is, the Fanaroff–Riley (FR) classification (e.g., Baum et al. 1995). It is proposed that FSRQs and all or some LBLs are beamed counterparts to FR type II radio galaxies with high luminosity, and IBLs, HBLs, and possibly some LBLs are counterparts to FR type I objects with low luminosity (Meyer et al. 2011; Giommi et al. 2012). Giommi et al. (2012) report that known LBLs are inhomogeneous and contain both FR I and II subtypes.

The variability characteristics of the flux and polarization have also been discussed for the different subtypes of blazars, particularly for the optical waveband in which all subtypes have been frequently monitored. It is well known that the optical activity apparently depends on ν_{peak} ; LSP blazars are more variable than HSP blazars (e.g., Bauer et al. 2009; Ikejiri et al. 2011; Hovatta et al. 2014). A similar ν_{peak} dependence has also been reported in the polarization variations, though the number of previous studies is limited (Itoh et al. 2016; Angelakis et al. 2016). The mechanism of the effect of ν_{peak} on the observed flux and polarization variability is unclear. High- ν_{peak} objects show less activity, possibly because a large number or large area of emitting regions blur each short flare (Marscher & Jorstad 2010; Itoh et al. 2016; Angelakis et al. 2016), or possibly because

the jet volume fraction of a slower “sheath” component increases (Ghisellini et al. 2005; Itoh et al. 2016).

In this paper we focus on blazar variability. We have performed photometric and polarimetric monitoring of blazars using the 1.5 m Kanata telescope in Hiroshima since 2008 (Ikejiri et al. 2011; Itoh et al. 2016). The present study has two major objectives: to establish the observational features of the flux and polarization variability for characterizing the subtypes, and thereby to investigate the nature of the subtypes, for example, whether FSRQs and LBLs have a common origin and whether the jet structure of FSRQs is different from that of BL Lac objects. Our analyses can be divided into two parts, the extraction of features from the observed time series data and the selection of the features which are discriminative for the two subtypes. For the feature extraction, in past studies the blazar variability was occasionally characterized only by the features based on the variance of the whole data, while the variation timescale was not considered. We use the Ornstein–Uhlenbeck (OU) process to estimate both the timescale and the amplitude from the data. The OU process and more advanced models based on it have been used to characterize the variations observed in AGN and also in blazars (Kelly et al. 2009, 2011; Ruan et al. 2012; Sobolewska et al. 2014). For the feature selection we propose a data-driven approach to select the best set of features for classifying blazars by maximizing the generalization error of a classifier.

The structure of this paper is as follows: In section 2 we describe the data (subsection 2.1) and methods used in this paper, namely, the OU process for feature extraction (subsection 2.2) and sparse multinomial logistic regression for the classifier (subsection 2.3). In section 3 we present the results of the feature selection. In section 4 we evaluate the classifier and discuss the implications for the selected features.

2 Data and methods

2.1 Data

We used the data obtained with the Kanata telescope which was published in Itoh et al. (2016). The data includes V-band time series photometric and polarimetric data for 45 blazars from 2008–2014. Figure 1 shows examples of light curves and variations in the degree of polarization (PD).

Panels (a), (b), and (c) of figure 1 show examples of FSRQs: PKS 1510–089 and 3C 454.3 in 2010 and in 2008, respectively. The peak-to-peak amplitudes in the light curves are large, over 2 mag in all cases, while the light curve profiles are diverse: a solitary, short flare appears in panel (a), while a number of short flares superimposed on long outbursts appear in panels (b) and (c). The light curves change their apparent characteristics year by year

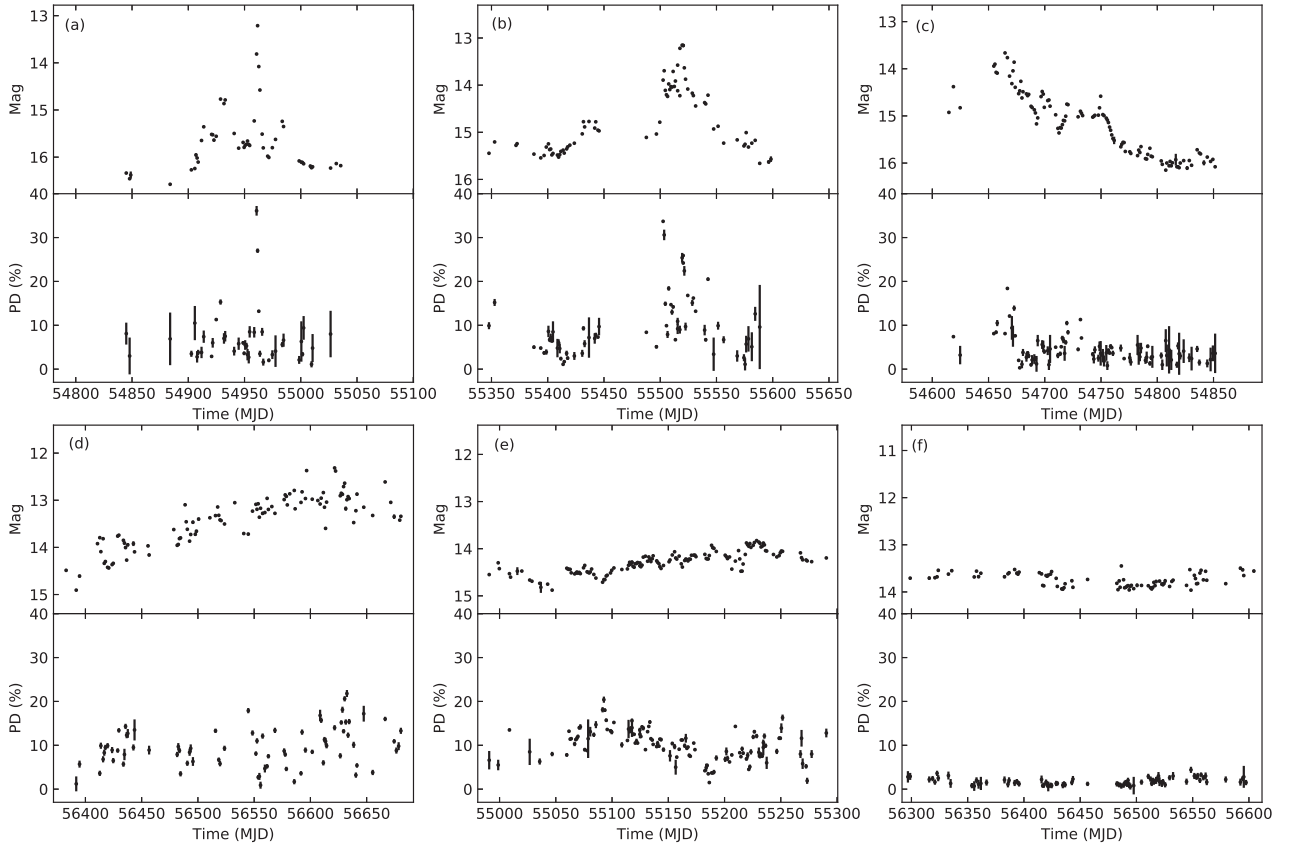


Fig. 1. Examples of light curves and PD time series data used in this paper. (a) PKS 1510–089 (FSRQ); (b) and (c) 3C 454.3 (FSRQ) in 2010 and 2008, respectively; (d) BL Lac (LBL) in 2013; (e) 3C 66A (IBL) in 2009; and (f) Mrk 501 (HBL). The upper and lower panels show the light curves and PD variations for each, respectively. The vertical and horizontal scales are common in all panels.

even for the same object, as shown in panels (b) and (c). Panels (d), (e), and (f) of figure 1 show examples of BL Lac objects: BL Lac (LBL), 3C 66A (IBL), and Mrk 501 (HBL), respectively. The peak-to-peak amplitude of the light curve in panel (d) is comparable to that of FSRQs, while the light curve profile looks different. The characterization and classification of these variations are the main subjects of this paper. The variation in polarization could give rise to some interesting features. For example, PD flares are associated with FSRQ flares, though no clear correlation can be seen in the light curve and PD variations in panels (d) and (e). Panels (e) and (f) show that the variation amplitude apparently decreases from LBL to HBL, as mentioned in the previous section.

2.2 Feature extraction with the OU process

We use the OU process for our time series analysis. The OU process is a stochastic model based on the multivariate normal distribution whose covariance between the data at time t_i and t_j , S_{ij} , is given as

$$S_{ij} = A_{\text{exp}} \exp\left(-\frac{|t_i - t_j|}{\tau}\right), \quad (1)$$

where τ and A_{exp} represent the characteristic variation timescale and amplitude at τ , respectively (Uhlenbeck & Ornstein 1930). For the time series data followed by the OU process, $f(t)$, the observed data, $m(t)$, is given by $m(t) = f(t) + \mathcal{N}(0, \sigma_{\text{OU}}^2)$, where the second term is the noise defined by the normal distribution having zero mean and variance σ_{OU}^2 . We can extract the characteristic features, A_{exp} , τ , and σ_{OU}^2 , from the observed time series data using the OU process regression.

The time series data introduced in subsection 2.1 have different observation periods for each object. The time series data of each object was divided into 1 yr segments, each of which is regarded as a sample in this paper. For modeling the light curves with the OU process, the magnitude values were translated to fluxes on a logarithmic scale, simply dividing by -2.5 . We assume that the light curves are approximated with the OU process with a characteristic timescale less than a few tens of days for our sample. The short timescale is supported by the data in which erratic variations are detected over measurement errors in all samples. If our assumption is true, the power spectrum should be flat for frequencies (f) lower than the characteristic frequency, and decays as f^{-2} for higher frequencies (Kelly et al.

2011). A strong linear trend in the time series data breaks this assumption because the power becomes larger in lower frequencies. We consider that the linear trend has an origin different from the short-term variations governed by the OU process. The presence of such distinct short- and long-term variations has been reported in AGN (Arévalo et al. 2006; McHardy et al. 2007; Kelly et al. 2011) and also in blazars (Sobolewska et al. 2014). Hence, we first subtracted the linear trend from the samples, and then performed the OU process regression. The slope value of the linear trend can be considered an indicator of the power at the lowest frequencies, and we use it as a feature for the classification in the next section.

The OU process is identical to the Gaussian process with an exponential kernel. We used the Python package for the Gaussian process, GPy, which includes a package for the Markov chain Monte Carlo (MCMC) method for the estimation of the posterior probability distributions of the parameters. In the present work, we estimated the posterior distribution of A_{exp} with a flat prior probability, and that of τ with a positive flat prior. We fixed σ_{OU}^2 with a typical measurement error of the data. We estimated the posterior probability distributions of A_{exp} and τ using the MCMC method for each light curve sample. We set $\sigma_{\text{OU}}^2 = 10^{-5}$. Figure 2 shows trace plots of A_{exp} and τ , their posterior distributions, and the observed and model light curves for the sample S5 0716+714 between MJD 55050 and 55389. The MCMC samples converge to a stationary distribution and the posterior distributions have single-peaked profiles. In this case, we successfully obtained unique solutions of A_{exp} and τ .

On the other hand, we found that A_{exp} and τ were not uniquely determined for several of the samples, mainly because the data size is not large enough to make a meaningful estimate of the parameters. A significant number of the samples from Itoh et al. (2016) have only <30 data points. Even in the samples with larger data size, τ is not uniquely determined if it is too long. Figure 3 shows an example, AO 0235+16 between MJD 54617 and 54946. The MCMC samples do not converge to a stationary distribution and τ can be very large, reaching over 300 d. Kozłowski (2017) reports that the OU process model is degenerate when the baseline of the light curve sample is shorter than ten times τ . The result in figure 3 is probably an example of such a case.

In this paper we used only samples for which A_{exp} and τ were uniquely determined, as in figure 2. This selection reduces the number of samples to 38 for 18 objects. The selected samples include 12 samples for 8 FSRQs and 26 samples for 10 BL Lac objects. The samples are listed in table 3 in the Appendix. The designation of the objects to

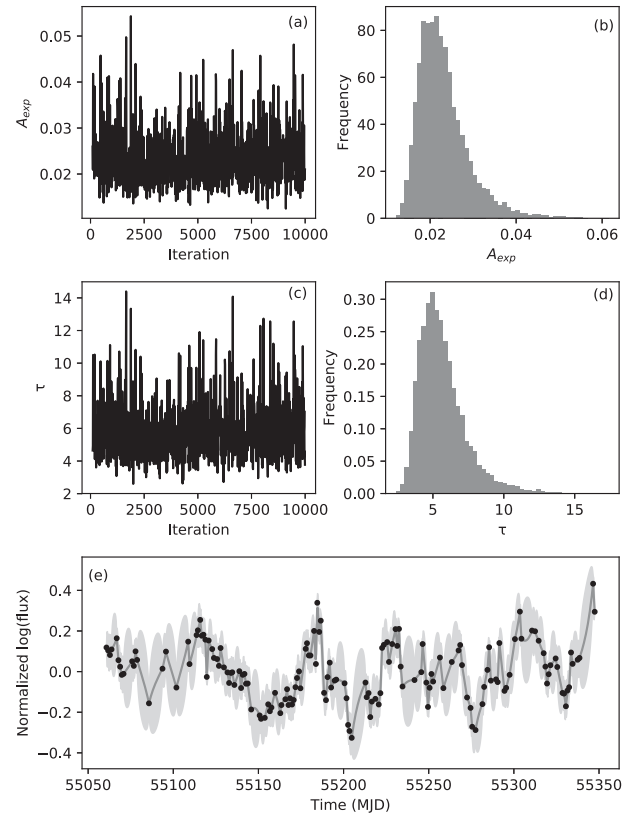


Fig. 2. Results of MCMC estimation of A_{exp} and τ for the sample S5 0716+714 between MJD 55050 and 55389. Panels (a) and (c) are the trace plots of the MCMC samples of A_{exp} and τ , respectively. Panels (b) and (d) are their posterior probability distributions. Panel (e) is the observed and model light curves. The filled circles are the data, and the solid line and shaded region indicate the mean of the model prediction and its 95% confidence interval, respectively. This is an example in which both A_{exp} and τ are uniquely determined.

the subtypes FSRQ, LBL, IBL, and HBL is taken from Itoh et al. (2016).

Blazars occasionally exhibit large prominent flares, as shown in panel (a) of figure 1, which definitely arise from a non-stationary process, whereas the OU process model assumes a stationary stochastic process. In order to characterize the non-stationarity, we calculate the cross-validation error (CVE) using the OU process regression, as follows: first, the sample is divided into 25 d bins, a subsample of which is for validation while the others are for training. Then, the OU process regression is performed with the training subsets. Then, the log-likelihood is calculated from the validation subset and the optimized model. Using the other subsamples as validation data, we obtained about 10 log-likelihoods for each sample. The CVE is defined as their mean. A large CVE means that the validation data has a large deviation from the prediction of the model constructed from the training data. Hence, a large value of CVE indicates a high degree of non-stationarity.

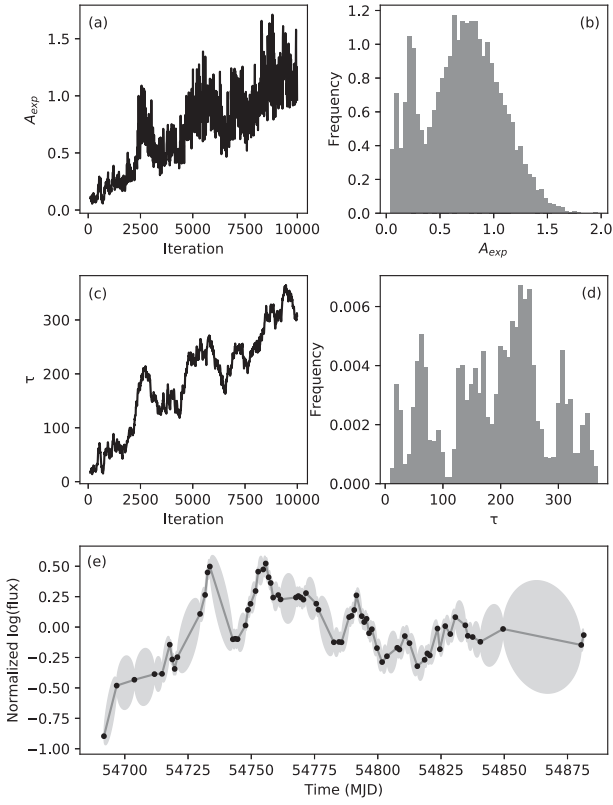


Fig. 3. As figure 2 but with the light curve data of AO 0235+16 between MJD 54617 and 54946. This is an example in which τ is too long.

The analysis of the time series PD data was performed in the same manner as for the light curves, that is, dividing it into 1 yr segments and converting to a logarithmic scale whose linear trends were subtracted. The OU process parameter σ_{OU}^2 was fixed to 10^{-4} . A_{exp} and τ were uniquely determined for the PD variations in all the samples except for seven. An example of one of the seven samples is shown in figure 4. Although A_{exp} is uniquely determined, the MCMC samples of τ do not converge, and τ can be quite small (note that the scale of τ is logarithmic in figure 4). As a result, the model of PD is simply the mean of the data, as shown in panel (e). These results suggest that the characteristic timescale is too short to be properly determined with our data. We set $\tau = 0.0$ for the seven samples. While a value of zero for τ is physically undefined, it works for training and evaluating the classifier representing very short timescales. CVEs were also calculated for the PD data. In addition, we also used the median of the PD as a feature parameter.

In total, we obtained nine features from the light curve and PD data: the four features from the light curve samples, A_{exp} , τ , the slope of the linear trend, and CVE, and five features from the PD samples, A_{exp} , τ , linear slope, CVE, and PD median. The values of the features are listed in table 3 in the Appendix.

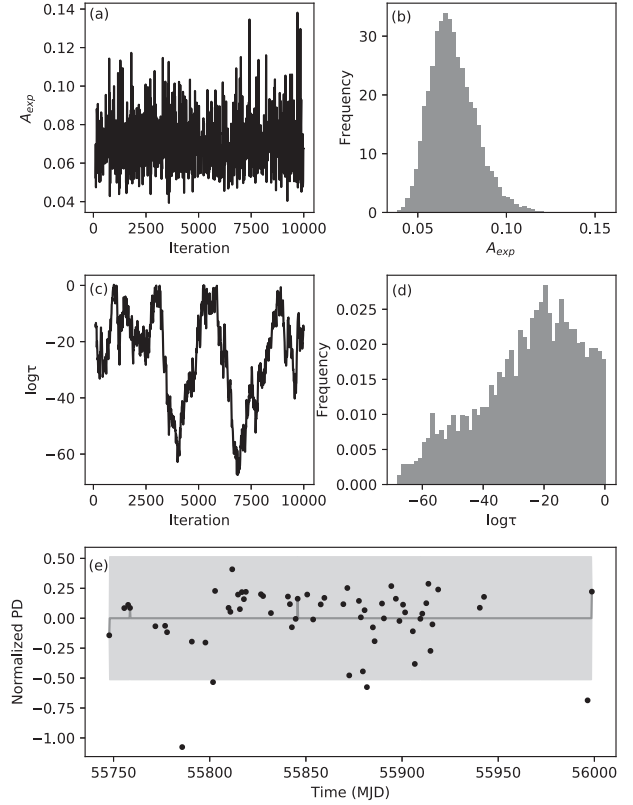


Fig. 4. As figure 2 but with the PD data of S5 0716+714 between MJD 55746 and 56125. Note that the scale of τ is logarithmic. This is an example of PD analysis in which τ is too short.

2.3 Sparse multinomial logistic regression

We construct a classifier for FSRQs and BL Lac objects based on the nine features described in subsection 2.2. We use sparse multinomial logistic regression (SMLR) to determine the classifier (Krishnapuram et al. 2005). We consider the problem of defining an M -class classifier with N labeled samples, each of which has a K -dimensional feature vector, $\theta_i = \{\theta_{i,1}, \theta_{i,2}, \dots, \theta_{i,K}\} (i = 1, 2, \dots, N)$. A sample that belongs to the j th class can be expressed with a vector $y = \{y^{(1)}, y^{(2)}, \dots, y^{(M)}\}$ such that $y^{(j)} = 1$ and the other elements are 0. Multinomial logistic regression gives the probability that a sample belongs to the j th class as

$$P(y^{(j)} = 1 | \theta, w) = \frac{\exp(w^{(j)T} \theta)}{\sum_{j=1}^M \exp(w^{(j)T} \theta)}, \quad (2)$$

where $w^{(j)}$ is the weight vector for the j th class. The log-likelihood function is given by the data θ as

$$\ell(w) = \sum_{i=1}^N \log P(y_i | \theta_i, w). \quad (3)$$

Then, the solution of SMLR is expressed as

$$\hat{\mathbf{w}} = \arg \max_{\mathbf{w}} \{\ell(\mathbf{w}) - \lambda \|\mathbf{w}\|_1\}, \quad (4)$$

where $\|\mathbf{w}\|_1$ is the ℓ_1 norm, $\|\mathbf{w}\|_1 = \sum_i |w_i|$, and λ is a sparsity parameter that controls the complexity of the model.

SMLR gives a linear classifier against the observed features if it is used as θ . In this case, SMLR can select the important features because the ℓ_1 term makes \mathbf{w} sparse. On the other hand, a nonlinear classifier can be obtained if the observed features are transformed with nonlinear kernel functions. Then, we can avoid over-fitting due to the ℓ_1 term. In the present study, the features listed in table 3 were normalized and the feature vector of the i th sample, \mathbf{x}_i , was obtained. The j th element of θ_i was obtained from \mathbf{x}_i and \mathbf{x}_j with the RBF kernel as follows:

$$\theta_{i,j} = \exp \left\{ -\frac{|\mathbf{x}_i - \mathbf{x}_j|^2}{2\sigma_{\text{RBF}}^2} \right\}, \quad (5)$$

where σ_{RBF}^2 is the bandwidth.

As mentioned in subsection 2.2, the number of samples, N , is 38. The number of classes, M , is two: FSRQs and BL Lac objects. Because of the small sample size, the three subtypes LBL, IBL, and HBL are combined as one BL Lac type, while the characteristics of the subtypes are discussed in subsection 4.2. The classifier is evaluated from the so-called “area under the curve” (AUC), which is defined by the receiver operating characteristic curve. The simple accuracy of the classifier is inadequate because the number of BL Lac objects is larger than the number of FSRQs in our sample (12 FSRQ samples and 26 BL Lac samples). The AUC is calculated by leave-one-out cross validation for estimating the generalization error of the classifier. Optimization of the model and the calculation of the cross-validated AUC were performed with the Java-based application SMLR.¹

3 Results

We investigate the features that are discriminative for FSRQs and BL Lac objects based on SMLR and cross-validated AUC using the nine features obtained from the data. SMLR has two hyperparameters, σ_{RBF}^2 and λ . We first consider appropriate values for these two parameters for our study.

A small σ_{RBF}^2 leads to a complicated model with a large number of samples retained in the classifier. Such a small σ_{RBF}^2 occasionally creates an island-like boundary. Figure 5 shows examples of the probability map of BL Lac-type samples calculated with $\sigma_{\text{RBF}}^2 = 1.0$ (left panel) and 5.0 (right panel) using two features, the light curve CVE and PD

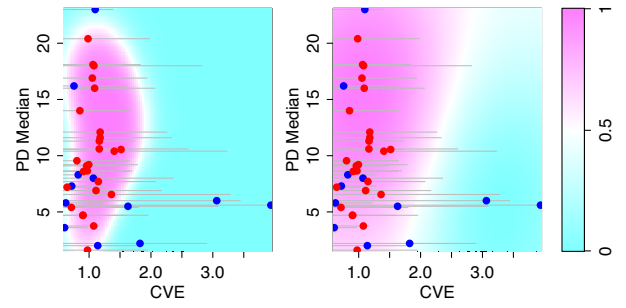


Fig. 5. Examples of complicated and simple boundaries. The color map indicates the probability map of a BL Lac-type sample calculated from the light curve CVE and PD median with SMLR. The left and right panels show those obtained with bandwidth parameters of 1.0 and 5.0, respectively. The blue and red circles indicate FSRQ and BL Lac samples. (Color online)

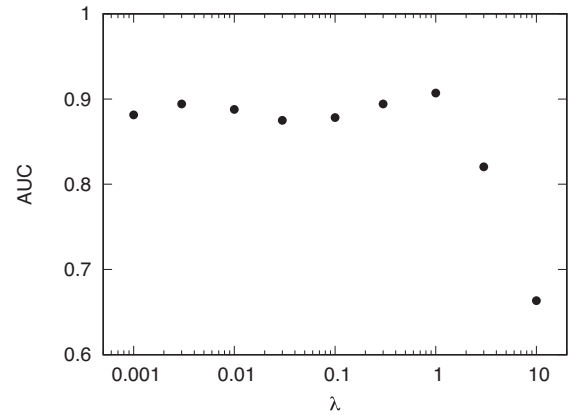


Fig. 6. Optimal AUC against λ .

median. We set $\lambda = 0.1$ in this case. As can be seen in the left panel, the high-probability region forms an “island” within the surrounding low-probability area. However, it is unlikely that the two subtypes of blazars have such a complicated boundary. A linear or slightly nonlinear model, like that in the right panel, is more reasonable. We confirmed that a classifier with large bandwidths ($\sigma_{\text{RBF}}^2 \gtrsim 5$) does not have an island-like boundary using our samples. In the following analysis, we set $\sigma_{\text{RBF}}^2 = 5.0$.

The sparsity parameter, λ , also controls the complexity of the model. We investigated the best AUC of all combinations of the nine features against various values of λ . The result is given in figure 6, showing that AUC becomes maximum around $\lambda = 1.0$. A model obtained with $\lambda > 1$ is too simple to appropriately classify the samples. On the other hand, a small λ (< 1) leads to over-fitting. We set $\lambda = 1.0$ in the following analysis.

We made an exhaustive test of all the parameters to find the most important features (e.g., Igarashi et al. 2018). The number of combinations of the nine features is $2^9 - 1 = 511$. Using SMLR, we developed 511 classifiers using models with different combinations of parameters, and

¹ (<http://www.cs.duke.edu/~amink/software/smlr>).

calculated the AUCs for each. Table 1 lists the top 20 classifiers in order of AUC values. For example, the classifier with the highest AUC ($=0.923$) uses six features: the CVE, A_{exp} , and τ of the light curve, and the median, CVE, and τ of the PD. It has an accuracy of 0.842. As can be seen in the table, the correlation between the accuracy score and AUC is low in the 20 models. This is probably due to the small sample size, and indicates that a small difference in the AUC is not important. We found that the CVE and A_{exp} of the light curve are used in all the top 20 models, and that τ of the light curve and PD median are used in 19 models. This result suggests that these four features are essential to classifying FSRQs and BL Lac objects.

The probability of the BL Lac type (P_{BL}) for each sample obtained with the classifier using the four parameters is listed in table 3 in the Appendix. We can determine the class of each sample based on P_{BL} . Table 2 is the error matrix for several different decision criteria: $P_{\text{BL}} = 0.5, 0.6$, and 0.7 . In the case of $P_{\text{BL}} = 0.5$, all the samples classified as FSRQs are indeed FSRQs (accuracy $=1.0$). On the other hand, only six of the 12 FSRQs are correctly classified as FSRQ, while the other six samples are misidentified. The BL Lac prediction accuracy improves with increased decision criterion (P_{BL}), while the prediction accuracy of FSRQs decreases in that case. The high rate of misidentified FSRQs suggests that a significant portion of FSRQs cannot be distinguished from BL Lac objects based on the four features.

Table 2. Error matrix and accuracy.

	Reference		
Classification	BL Lac	FSRQ	Accuracy
	$P_{\text{BL}} = 0.5$		
BL Lac	26	6	0.81
FSRQ	0	6	1.00
	$P_{\text{BL}} = 0.6$		
BL Lac	25	4	0.86
FSRQ	1	8	0.89
	$P_{\text{BL}} = 0.7$		
BL Lac	21	3	0.88
FSRQ	5	9	0.64

4 Discussion

4.1 Significance of the classifier

A good classifier could incidentally be obtained in high-dimensional problems even if all the features are not related to the real characteristics of the samples. We tested the significance of the obtained classifier described in the previous section using artificial data sets. The sets of artificial data consist of 12 FSRQs and 26 BL Lac objects, as for the case in table 3, with random values for the nine features. The random numbers were uniformly distributed between 0 and 1. We made 100 sets of data and obtained $511 \times 100 = 51100$ AUC values, in the same manner as described in

Table 1. Variables used, AUC, and accuracy of top 20 models.*

Light curve				Polarization degree				AUC	Accuracy
CVE	Slope	A_{exp}	τ	Median	CVE	Slope	A_{exp}		
•	—	•	•	•	—	•	—	0.907	0.842
•	•	•	•	•	—	—	—	0.904	0.816
•	•	•	•	•	—	•	—	0.888	0.842
•	•	•	•	•	—	—	•	0.885	0.789
•	•	•	•	•	•	—	—	0.881	0.868
•	—	•	•	•	—	•	—	0.881	0.737
•	•	•	•	•	•	•	•	0.878	0.816
•	—	•	•	•	•	•	—	0.878	0.789
•	—	•	•	•	•	—	•	0.875	0.789
•	•	•	•	•	•	—	•	0.872	0.789
•	•	•	•	•	•	—	—	0.872	0.816
•	•	•	•	•	•	•	—	0.869	0.842
•	—	•	•	—	•	—	—	0.865	0.842
•	•	•	•	•	•	•	•	0.862	0.763
•	•	•	•	•	—	•	—	0.862	0.737
•	•	•	—	•	—	•	•	0.859	0.789
•	•	•	•	•	—	•	•	0.856	0.763
•	—	•	•	•	•	•	•	0.856	0.763
•	•	•	•	•	•	•	—	0.853	0.816
•	•	•	•	•	•	—	•	0.853	0.789

*A bullet symbol indicates the parameter was included in that model.

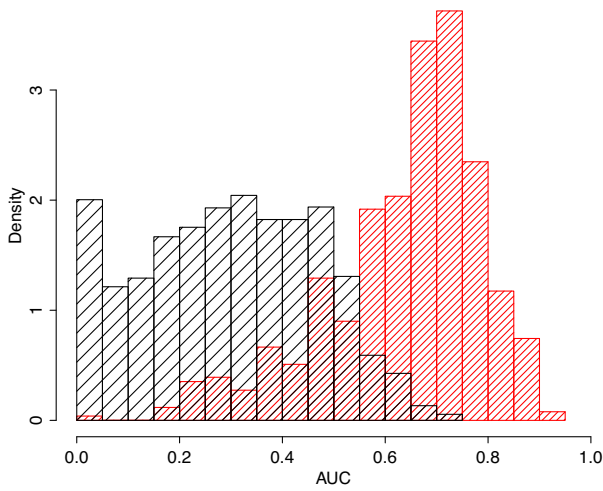


Fig. 7. Histograms of the AUC obtained from real samples (red) and artificial data generated from random numbers (black). See the text for details. (Color online)

the previous section. Figure 7 shows histograms of the AUC values from the real and artificial samples. The distribution from the real samples exhibited systematically higher AUCs than that of the random data sets. The AUC values obtained from the random data sets are concentrated in the area $AUC < 0.8$. Thus, it is unlikely that the obtained best AUC values from the real data (~ 0.9) are incidentally obtained.

4.2 Implications from the four features

Here, we discuss the implications of the results of section 3. Figure 8 shows scatter plots of the four features. The correctly classified FSRQs ($P_{BL} < 0.5$) are indicated by the filled blue circles, while the misclassified FSRQs are indicated by the open circles. As can be seen from the top panel, the correctly classified FSRQs have high CVE and/or high A_{exp} , while the misclassified FSRQs have values for these features comparable to those of the BL Lac objects. The high value of CVE indicates the presence of prominent non-stationary flares which deviate from the stationary OU process. The high value of A_{exp} indicates a large amplitude of variation at the characteristic timescale, τ . We propose that FSRQs are characterized by rare and large flares which have a time series structure distinct from ordinary variations. If the frequency of the flares is relatively high, a few times a year say, then the light curve can be reproduced by the OU process with a high A_{exp} . If the frequency is low, such as once a year, then the light curve can be divided into two distinct periods, that is, the stationary state and the non-stationary flare, which causes a high CVE. The misclassified FSRQs may be objects in which the flare frequency was so low that no flare was detected in the year.

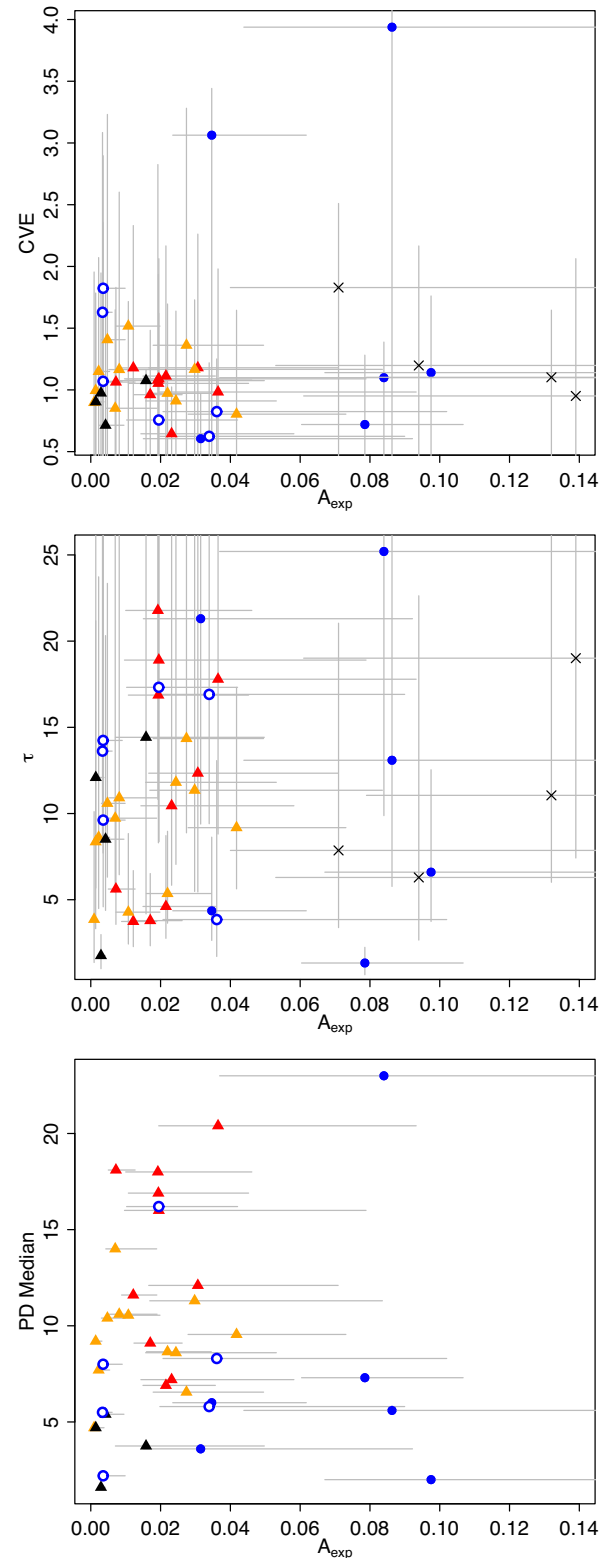


Fig. 8. Scatter plots of the selected features. The top, middle, and bottom panels show CVE, τ , and PD median against A_{exp} , respectively. The blue filled and open circles denote the correctly classified and misclassified FSRQ samples, respectively. The red, orange, and black triangles are LBL, IBL, and HBL samples, respectively. The gray bars represent the 95% confidence intervals. The crosses are the results obtained from the X-ray data of the HBL Mrk 421. (Color online)

It is not evident that the characteristics of the light curve CVE and A_{exp} originate from a different structure and/or physical condition for the jets between the blazar subtypes (e.g., Itoh et al. 2016). It is possible that it is simply due to the ν_{peak} effect. In order to investigate this point, we analyzed the X-ray data of the HBL Mrk 421 using the X-ray light curve presented in Yamada et al. (2020). The data was obtained with XRT/Swift from 2009 to 2014. The time interval of the X-ray light curve is 1 d. We analyzed the data in the same manner as for the optical light curves, that is, dividing it into 1 yr segments, calculating the flux density in a logarithmic scale whose linear trends were subtracted, and performing the OU process regression for each segment. Table 4 in the Appendix shows the estimated CVE, A_{exp} , and τ for each sample. We successfully obtained values for the four segments listed in the table. We could not obtain those values for the segment MJD 55939–56078, mainly because of the small sample size ($N = 34$). The estimated values are indicated by crosses in the top and middle panels of figure 8. They are definitely in the regime of FSRQs, especially regarding the large A_{exp} . This result suggests that the large A_{exp} does not originate from different jet properties in the blazar subtypes, but from the ν_{peak} effect.

The variation timescale of the light curve, τ , was also selected as an important feature for classification. However, as shown in the middle panel of figure 8, we cannot find any clear differences between the τ distributions of FSRQs and BL Lac objects. This feature was selected mainly because it is useful for the classification of only one FSRQ sample, 3C 454.3 in MJD 54542–54930. This sample has a small CVE ($=0.60$) and a not very high A_{exp} ($=3.15$), from which the object cannot be distinguished from BL Lac objects, but has an exceptionally large τ ($=21.30$). We consider that our analysis does not provide enough evidence to determine the importance of τ .

It is proposed that the beaming factor of FSRQs is systematically larger than that of BL Lac objects. Giommi et al. (2012) proposed that the two subtypes have a common nature, except for the beaming factor. Itoh et al. (2016) proposed that the jet volume fraction occupied by the fast “spine” should be larger in FSRQs than BL Lac objects. The difference in the beaming factor would also change the characteristics of the variability. For example, a shorter variation timescale is expected with a higher beaming factor. However, our analysis provides no strong evidence that τ for FSRQs is systematically smaller than for BL Lac objects, while the uncertainty of τ is large.

In the bottom panel of figure 8, we can see a trend that BL Lac objects have high PD medians compared with FSRQs. This characteristic is stronger when HBLs (the black triangles in the figure) are neglected. The low PD medians of HBLs are probably due to a large contamination of the unpolarized emission from their host galaxies (Shaw

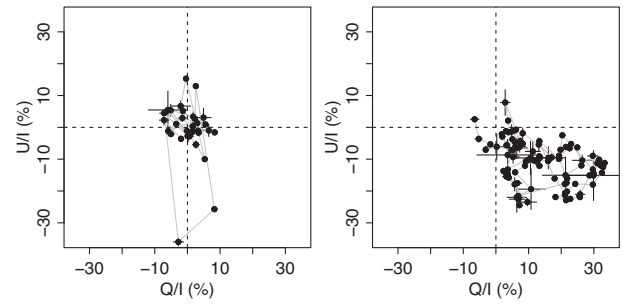


Fig. 9. Polarization variations in the Stokes Q/I – U/I plane of the FSRQ PKS 1510–089 in MJD 54759–55124 (left) and the LBL OJ 287 in MJD 55045–55451 (right).

et al. 2013). Figure 9 shows examples of polarization variations in the Stokes Q/I – U/I plane. The left and right panels show the data of the FSRQ PKS 1510–089, which has a low PD median, and that of the LBL OJ 287, which has a high PD median, respectively. An increase in PD is occasionally associated with the flares of blazars, and in general the PD remains relatively low when the object is faint. In the left panel of figure 9 most of the data points exhibit low PDs, except for a few data points with high PDs $>20\%$, which are associated with the prominent flare shown in panel (a) of figure 1. The high value of the PD median in BL Lac objects indicates that PD is relatively high even in the faint state. The right panel of figure 9 shows an example: the object had a relatively high PD throughout the year. It has been proposed that the LBL object BL Lac has two polarization components: short-term variations superimposed on a stable or semi-stable component (Hagen-Thorn et al. 2002; Sakimoto et al. 2013). The fact that the PD median was selected in our analysis suggests that the presence of a stable polarization component is a characteristic feature of BL Lac objects.

The origin of the PD median characteristic is unclear. The values of the PD median apparently correlate with ν_{peak} in BL Lac objects, being lowest in HBLs and highest in LBLs. However, FSRQs have low PD medians, although they have the highest ν_{peak} . Hence, the characteristic is not due to the ν_{peak} effect, but possibly due to a difference in the jet structure between the blazar subtypes. In this case, the stable polarization component should have a different emitting site or physical condition from the short-term variations since the characteristics of the short-term flux variability can be interpreted as the ν_{peak} effect, as discussed above. The presence of the stable component may suggest that the accelerated electrons have a long lifetime with a long cooling timescale. According to Kaspi et al. (2005), the size of the broad line region (BLR) has a positive correlation with the AGN luminosity, and the AGNs with the highest luminosity have large BLRs up to sub-parsec scale. FSRQs form a subgroup of blazars with the highest luminosity, not only of the jets, but also of the AGNs (Fossati et al. 1998;

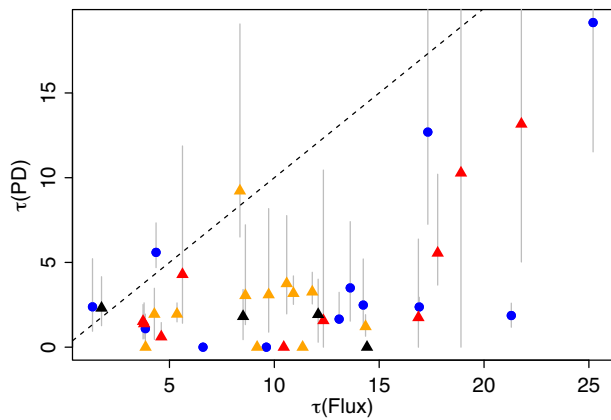


Fig. 10. Correlations of the flux and PD τ . The blue circles and the red, orange, and black triangles denote the FSRQ, LBL, IBL, and HBL samples, respectively. The dashed line indicates $\tau(\text{PD}) = \tau(\text{Flux})$. (Color online)

Shaw et al. 2013; Ghisellini et al. 2017). The lack of a stable component in FSRQs may be reconciled with the presence of a strong radiation field induced by a large BLR causing strong Compton cooling of the electrons even in the sub-parsec region, which is the source of the stable polarization component in BL Lac objects.

Giommi et al. (2012) reported that LBLs include both low-luminosity FR I objects and high-luminosity FR II objects. If this is the case, there may be LBLs with a low PD median. Our samples included only two LBL objects, BL Lac and OJ 287. The number of samples is so small that we cannot make conclusions about the population of LBLs. Further studies are required to understand the relationship between the presence/absence of the stable polarization component and FR types or AGN luminosity.

4.3 Features of polarization variability

In this paper we used features derived from both the light curves and PD variations, while the only PD feature selected as being useful for classifying FSRQs and BL Lac objects was the PD median. Figure 10 shows a scatter plot of τ of the light curve and of the PD variations. In this figure we can see that the timescale of the PD variation tends to be shorter than that of the light curve. Most of the objects have a PD τ shorter than 5 d. As mentioned in subsection 2.2, the PD τ was too short to be uniquely determined in seven cases. These results imply that the real τ could be too short to be correctly estimated from our data. If this is the case, the PD features were not selected in our analysis possibly because they were not good indicators for the nature of the PD variability. The fact that the PD τ is significantly shorter than the light curve τ suggests that the relaxation timescale of the ordered magnetic field is shorter than the cooling timescale of the accelerated electrons.

On the other hand, the presence of a stable polarization component in BL Lac objects can also cause a lack of PD variation features in the selected features. The observed Stokes parameters are a sum of those of multiple components. If the contamination of the stable component is strong, the PD variation of a flare is diluted by the stable component. For example, the increase in PD associated with a flare is canceled if the direction of polarization of the flare component is perpendicular to that of the stable component. This effect also causes the PD features to be poor indicators of the real PD variability. In future work we will extract the features of the PD variation for both the short-term flares and the stable, or long-term, variation component by separating these components (Uemura et al. 2010).

5 Summary

We characterized the optical variability of blazars using the OU process and investigated the features which are discriminative for the two blazar subtypes, FSRQs and BL Lac objects. Our summarized findings are as follows:

- Four features, namely the variation amplitude, A_{exp} , characteristic timescale (τ), and non-stationarity (CVE), from the light curve and the PD median are essential in classifying blazars into FSRQs and BL Lac objects.
- FSRQs are characterized by rare and large flares based on a large A_{exp} and/or CVE. We found that the X-ray variability of the HBL Mrk 421 also has large A_{exp} , comparable to the optical variability of FSRQs. Hence, the characteristics of A_{exp} and CVE are governed not by the differences in the jet structure between the subtypes, but by the ν_{peak} effect.
- The high PD median of BL Lac objects suggests that they tend to have a stable polarization component. The lack of such a component in FSRQs is possibly due to strong Compton cooling from a large BLR in sub-parsec-scale jets.
- The variation timescale of PD is significantly shorter than that of the light curves. This may indicate that the relaxation timescale of the ordered magnetic field is shorter than the cooling timescale of the accelerated electrons.

Acknowledgments

This work was supported by a Kakenhi Grant-in-Aid (No. 25120007) from the Japan Society for the Promotion of Science (JSPS).

Appendix Samples and features

Table 3 presents the description of the samples and their nine features. Table 4 presents those of the X-ray data of Mrk 421.

Table 3. Samples and features for classification

Object	MJD		Light curve				Polarization degree							
	Start	End	N	CVE	Slope ($\times 10^{-4}$)	A_{exp} ($\times 10^{-2}$)	τ	Median	CVE	Slope ($\times 10^{-3}$)	A_{exp} ($\times 10^{-2}$)	τ	Type	P_{BL}
S2 0109+22	54581	54974	69	1.52 $^{+0.20}_{-0.17}$	6.00 \pm 2.23	1.08 $^{+0.91}_{-0.36}$	4.28 $^{+4.56}_{-1.85}$	10.55	1.18 $^{+0.57}_{-0.11}$	-2.08 \pm 0.65	7.12 $^{+3.31}_{-2.00}$	1.95 $^{+1.53}_{-1.49}$	IBL	0.86
	54612	54974	114	1.16 $^{+1.47}_{-1.44}$	-0.86 \pm 1.11	0.82 $^{+1.09}_{-0.30}$	10.91 $^{+16.11}_{-4.46}$	10.60	1.24 $^{+0.35}_{-0.17}$	-2.72 \pm 0.26	6.63 $^{+0.79}_{-0.79}$	3.17 $^{+1.03}_{-0.65}$	IBL	0.86
	54974	55345	142	1.41 $^{+1.12}_{-1.27}$	9.57 \pm 0.66	0.48 $^{+0.31}_{-0.17}$	10.59 $^{+12.76}_{-4.28}$	10.40	1.02 $^{+0.40}_{-0.94}$	-0.86 \pm 0.23	6.71 $^{+2.40}_{-1.05}$	3.75 $^{+4.01}_{-1.79}$	IBL	0.85
	55345	55671	72	0.85 $^{+0.80}_{-0.79}$	-2.03 \pm 1.28	0.70 $^{+1.19}_{-0.78}$	9.73 $^{+17.90}_{-15.82}$	14.00	1.31 $^{+1.17}_{-0.43}$	1.03 \pm 0.24	6.54 $^{+2.02}_{-1.93}$	3.10 $^{+3.08}_{-2.31}$	IBL	0.90
3C 66A	55671	56073	30	1.00 $^{+0.79}_{-0.90}$	3.65 \pm 1.17	0.14 $^{+0.35}_{-0.09}$	8.36 $^{+12.82}_{-5.94}$	9.20	1.32 $^{+0.63}_{-0.16}$	-4.66 \pm 1.55	7.21 $^{+9.20}_{-4.56}$	9.22 $^{+9.85}_{-4.17}$	IBL	0.85
	56409	56797	56	1.15 $^{+0.80}_{-0.80}$	-4.31 \pm 1.06	0.23 $^{+0.39}_{-0.09}$	8.62 $^{+14.11}_{-4.13}$	7.70	1.19 $^{+1.06}_{-0.35}$	-1.45 \pm 0.25	5.95 $^{+0.86}_{-0.35}$	3.05 $^{+4.17}_{-1.72}$	IBL	0.81
	54665	55050	138	1.36 $^{+1.92}_{-1.32}$	-8.45 \pm 1.57	2.74 $^{+2.21}_{-0.96}$	14.35 $^{+11.99}_{-5.47}$	6.55	1.14 $^{+0.85}_{-0.96}$	-0.11 \pm 0.28	6.66 $^{+2.24}_{-1.53}$	1.22 $^{+0.70}_{-0.57}$	IBL	0.68
	55050	55389	156	0.97 $^{+0.72}_{-0.84}$	-7.20 \pm 1.39	2.20 $^{+1.26}_{-0.61}$	5.36 $^{+3.61}_{-1.72}$	8.65	1.15 $^{+0.67}_{-0.93}$	0.57 \pm 0.32	7.07 $^{+2.60}_{-1.80}$	1.95 $^{+0.66}_{-0.46}$	IBL	0.83
S5 0716+714	55389	55746	98	0.91 $^{+0.73}_{-0.76}$	-17.70 \pm 1.84	2.44 $^{+2.88}_{-0.87}$	11.81 $^{+15.96}_{-4.76}$	8.60	1.18 $^{+0.80}_{-0.10}$	0.54 \pm 0.38	7.00 $^{+2.98}_{-1.79}$	3.26 $^{+1.16}_{-0.71}$	IBL	0.79
	55746	56125	98	0.80 $^{+0.84}_{-0.76}$	10.99 \pm 2.16	4.18 $^{+3.13}_{-1.38}$	9.18 $^{+8.14}_{-3.98}$	9.55	1.18 $^{+0.21}_{-0.11}$	-2.09 \pm 0.60	6.82 $^{+2.51}_{-1.62}$	0.00	IBL	0.78
	56484	56868	51	1.17 $^{+1.10}_{-1.00}$	16.45 \pm 3.37	2.98 $^{+1.29}_{-0.58}$	11.35 $^{+5.87}_{-2.98}$	11.30	1.14 $^{+1.12}_{-0.68}$	0.32 \pm 0.52	7.03 $^{+2.02}_{-1.10}$	0.00	IBL	0.84
	54696	55045	100	0.98 $^{+0.84}_{-0.84}$	-12.39 \pm 1.77	3.65 $^{+1.70}_{-0.68}$	17.79 $^{+28.97}_{-8.98}$	20.40	1.16 $^{+1.06}_{-0.35}$	1.89 \pm 0.18	7.30 $^{+0.44}_{-0.44}$	5.55 $^{+4.65}_{-1.89}$	LBL	0.76
OJ 287	55045	55451	116	1.08 $^{+1.75}_{-1.04}$	-16.84 \pm 1.58	1.92 $^{+2.69}_{-0.92}$	21.78 $^{+31.06}_{-10.96}$	18.00	1.13 $^{+0.65}_{-1.10}$	-4.98 \pm 0.26	7.38 $^{+8.49}_{-1.93}$	13.17 $^{+33.42}_{-8.14}$	LBL	0.69
	55773	56161	42	1.09 $^{+1.07}_{-1.06}$	14.54 \pm 2.26	1.95 $^{+5.94}_{-0.99}$	18.90 $^{+63.15}_{-10.54}$	16.00	1.35 $^{+1.48}_{-1.23}$	2.64 \pm 0.75	7.18 $^{+10.63}_{-3.21}$	10.28 $^{+41.50}_{-10.28}$	LBL	0.77
	56488	56872	54	1.05 $^{+0.88}_{-1.01}$	5.73 \pm 2.77	1.94 $^{+2.59}_{-0.86}$	16.87 $^{+24.93}_{-8.57}$	16.90	1.27 $^{+1.14}_{-0.30}$	0.47 \pm 0.33	6.92 $^{+1.52}_{-0.68}$	1.75 $^{+4.63}_{-1.75}$	LBL	0.83
	55127	55438	36	1.08 $^{+0.08}_{-0.87}$	-23.73 \pm 2.76	1.58 $^{+3.39}_{-0.38}$	14.42 $^{+32.96}_{-10.24}$	3.75	1.16 $^{+0.30}_{-0.14}$	-0.49 \pm 0.78	5.48 $^{+6.63}_{-1.89}$	0.00	HBL	0.61
3C 279	54621	55115	58	0.76 $^{+0.70}_{-0.70}$	-38.92 \pm 2.62	1.95 $^{+0.98}_{-0.38}$	17.32 $^{+28.94}_{-8.94}$	16.20	1.06 $^{+0.37}_{-0.14}$	-5.09 \pm 0.65	7.69 $^{+3.36}_{-1.79}$	12.69 $^{+27.37}_{-5.44}$	FSRQ	0.81
	54568	55045	60	1.10 $^{+0.89}_{-0.79}$	6.85 \pm 2.19	8.40 $^{+26.42}_{-8.92}$	25.20 $^{+15.32}_{-7.36}$	23.00	1.05 $^{+0.88}_{-0.35}$	1.76 \pm 0.32	8.01 $^{+4.74}_{-2.41}$	19.15 $^{+28.63}_{-7.63}$	FSRQ	0.28
	54759	55124	50	3.94 $^{+3.89}_{-1.96}$	3.74 \pm 8.65	8.63 $^{+16.53}_{-4.25}$	13.09 $^{+27.36}_{-7.32}$	5.60	1.61 $^{+1.20}_{-1.20}$	-0.03 \pm 1.15	7.22 $^{+4.01}_{-2.44}$	1.66 $^{+1.58}_{-0.19}$	FSRQ	0.12
	54895	55490	99	1.63 $^{+1.46}_{-1.56}$	-0.63 \pm 0.42	0.34 $^{+0.28}_{-0.11}$	13.62 $^{+12.45}_{-5.07}$	5.50	1.09 $^{+0.40}_{-0.96}$	-0.28 \pm 0.22	6.38 $^{+5.46}_{-2.87}$	3.50 $^{+3.91}_{-1.96}$	FSRQ	0.66
RX J1542.8+612	56629	56956	50	0.90 $^{+0.70}_{-0.70}$	2.51 \pm 0.77	0.14 $^{+0.24}_{-0.06}$	12.09 $^{+22.26}_{-6.41}$	4.70	1.21 $^{+1.73}_{-1.08}$	-0.47 \pm 0.58	5.87 $^{+3.00}_{-1.57}$	1.93 $^{+2.08}_{-1.64}$	HBL	0.68
	56289	56660	84	0.97 $^{+0.97}_{-0.94}$	-1.73 \pm 0.76	0.29 $^{+0.12}_{-0.08}$	1.76 $^{+1.22}_{-0.66}$	1.60	1.22 $^{+1.34}_{-1.03}$	0.03 \pm 0.27	5.14 $^{+2.25}_{-1.18}$	2.31 $^{+1.83}_{-1.04}$	HBL	0.59
	55880	56780	77	1.14 $^{+0.78}_{-0.78}$	8.38 \pm 2.04	9.75 $^{+3.04}_{-3.04}$	6.60 $^{+2.86}_{-2.86}$	2.00	1.35 $^{+2.32}_{-1.01}$	-0.11 \pm 1.06	5.64 $^{+0.85}_{-0.85}$	0.00	FSRQ	0.25
	54555	54952	81	1.07 $^{+0.95}_{-0.95}$	2.78 \pm 1.00	0.35 $^{+0.35}_{-0.16}$	14.24 $^{+20.57}_{-6.53}$	8.00	1.14 $^{+1.01}_{-0.98}$	-0.10 \pm 0.19	5.90 $^{+0.32}_{-0.32}$	2.48 $^{+2.72}_{-1.38}$	FSRQ	0.76
1ES 1959+650	54577	54934	40	0.90 $^{+1.06}_{-0.86}$	5.76 \pm 0.94	0.10 $^{+0.16}_{-0.04}$	3.86 $^{+6.23}_{-2.50}$	4.70	1.16 $^{+1.07}_{-0.71}$	-0.26 \pm 0.55	5.73 $^{+1.21}_{-0.71}$	0.00	IBL	0.75
	54628	54925	57	0.71 $^{+1.08}_{-0.67}$	23.68 \pm 1.75	0.42 $^{+0.53}_{-0.18}$	8.51 $^{+11.81}_{-4.13}$	5.40	1.24 $^{+0.31}_{-0.22}$	0.10 \pm 0.55	5.92 $^{+0.93}_{-0.93}$	1.81 $^{+1.59}_{-1.37}$	HBL	0.74
	54537	54908	100	1.06 $^{+0.77}_{-0.98}$	-1.75 \pm 1.31	0.72 $^{+0.55}_{-0.22}$	5.62 $^{+5.15}_{-2.05}$	18.10	1.03 $^{+0.88}_{-0.73}$	-0.09 \pm 0.24	7.16 $^{+0.96}_{-0.96}$	4.29 $^{+2.08}_{-2.88}$	LBL	0.92
	54908	55270	104	1.18 $^{+1.15}_{-1.08}$	8.11 \pm 1.23	1.22 $^{+0.68}_{-0.44}$	3.74 $^{+2.95}_{-1.46}$	11.60	1.14 $^{+0.61}_{-0.58}$	-0.53 \pm 0.22	6.84 $^{+1.01}_{-0.70}$	1.52 $^{+0.99}_{-0.88}$	LBL	0.89
BL Lac	55270	55605	58	1.18 $^{+1.08}_{-0.88}$	-13.33 \pm 2.30	3.07 $^{+4.02}_{-3.51}$	12.34 $^{+17.89}_{-4.61}$	12.10	1.19 $^{+0.94}_{-0.58}$	1.49 \pm 0.47	6.84 $^{+3.31}_{-2.05}$	1.57 $^{+1.88}_{-1.57}$	LBL	0.84
	55605	56011	67	0.64 $^{+0.57}_{-0.57}$	0.85 \pm 2.28	2.32 $^{+0.88}_{-0.88}$	10.45 $^{+4.61}_{-1.85}$	7.20	1.14 $^{+0.58}_{-0.58}$	0.17 \pm 0.48	6.71 $^{+1.40}_{-1.40}$	0.00	LBL	0.76
	56011	56347	82	1.11 $^{+1.05}_{-1.05}$	-26.64 \pm 2.01	2.15 $^{+1.42}_{-0.66}$	4.61 $^{+4.11}_{-1.85}$	6.90	1.20 $^{+0.27}_{-0.18}$	-2.22 \pm 1.08	6.69 $^{+5.49}_{-3.65}$	0.61 $^{+0.84}_{-0.07}$	LBL	0.79
	56347	56735	100	0.96 $^{+0.52}_{-0.89}$	21.72 \pm 1.45	1.70 $^{+0.92}_{-0.47}$	3.79 $^{+2.73}_{-1.46}$	9.10	1.19 $^{+0.52}_{-0.52}$	0.63 \pm 0.35	6.86 $^{+2.80}_{-1.76}$	1.39 $^{+1.23}_{-0.87}$	LBL	0.85
CTA 102	56140	56339	41	0.82 $^{+0.43}_{-0.78}$	-40.03 \pm 9.38	3.61 $^{+6.59}_{-1.54}$	3.85 $^{+9.22}_{-2.14}$	8.30	1.87 $^{+2.25}_{-1.80}$	7.44 \pm 2.09	7.18 $^{+3.17}_{-1.92}$	1.09 $^{+0.86}_{-1.00}$	FSRQ	0.79
	54542	54930	108	0.60 $^{+0.36}_{-0.55}$	-39.57 \pm 1.84	3.15 $^{+6.07}_{-1.64}$	21.30 $^{+42.74}_{-10.21}$	3.60	1.29 $^{+0.55}_{-0.28}$	-1.01 \pm 0.51	6.41 $^{+2.35}_{-1.30}$	1.87 $^{+0.73}_{-0.69}$	FSRQ	0.39
	54930	55270	155	0.62 $^{+0.56}_{-0.56}$	16.01 \pm 1.65	3.39 $^{+3.60}_{-2.81}$	16.91 $^{+7.50}_{-3.43}$	5.80	1.32 $^{+0.46}_{-0.91}$	0.91 \pm 0.34	6.73 $^{+0.68}_{-0.70}$	2.37 $^{+0.40}_{-0.42}$	FSRQ	0.57
	55270	55795	91	0.72 $^{+0.93}_{-0.93}$	0.72 \pm 2.94	7.85 $^{+2.81}_{-1.81}$	1.33 $^{+0.90}_{-0.68}$	7.30	1.42 $^{+0.91}_{-1.00}$	0.45 \pm 0.32	7.23 $^{+0.51}_{-0.51}$	2.38 $^{+0.42}_{-1.44}$	FSRQ	0.48
3C 454.3	56000	56370	53	1.82 $^{+1.07}_{-1.79}$	10.97 \pm 1.34	0.36 $^{+0.63}_{-0.16}$	9.62 $^{+19.83}_{-5.03}$	2.20	1.19 $^{+0.38}_{-1.16}$	-0.82 \pm 4.32	5.81 $^{+9.51}_{-4.13}$	0.00	FSRQ	0.56
	56370	56744	78	3.06 $^{+0.38}_{-3.26}$	4.09 \pm 3.81	3.47 $^{+2.71}_{-1.12}$	4.36 $^{+4.27}_{-1.72}$	6.00	1.61 $^{+1.37}_{-1.24}$	0.48 \pm 0.83	7.21 $^{+1.74}_{-4.75}$	5.59 $^{+1.74}_{-0.90}$	FSRQ	0.37

Table 4. Samples and features of Mrk 421.

MJD	N	CVE	A_{exp}	τ
55150	55386	119	$1.10^{+0.54}_{-1.06}$	$0.13^{+0.20}_{-0.05}$
55533	55651	58	$0.95^{+1.11}_{-0.89}$	$0.14^{+0.30}_{-0.08}$
56268	56428	54	$1.83^{+0.68}_{-1.79}$	$0.07^{+0.08}_{-0.03}$
56627	56749	42	$1.20^{+0.97}_{-1.15}$	$0.09^{+0.18}_{-0.04}$
				$11.05^{+20.53}_{-5.04}$
				$19.01^{+38.48}_{-11.59}$
				$7.86^{+13.18}_{-4.48}$
				$6.29^{+16.34}_{-3.63}$

References

- Abdo, A. A., et al. 2010, *ApJ*, 716, 30
- Angelakis, E., et al. 2016, *MNRAS*, 463, 3365
- Arévalo, P., Papadakis, I. E., Uttley, P., McHardy, I. M., & Brinkmann, W. 2006, *MNRAS*, 372, 401
- Bauer, A., Baltay, C., Coppi, P., Ellman, N., Jerke, J., Rabinowitz, D., & Scalzo, R. 2009, *ApJ*, 699, 1732
- Baum, S. A., Zirbel, E. L., & O'Dea, C. P. 1995, *ApJ*, 451, 88
- Blandford, R. D., & Königl, A. 1979, *ApJ*, 232, 34
- Blandford, R. D., & Rees, M. J. 1978, in *BL Lac Objects*, ed. A. M. Wolfe (Pittsburgh: University of Pittsburgh Press), 328
- Fossati, G., Maraschi, L., Celotti, A., Comastri, A., & Ghisellini, G. 1998, *MNRAS*, 299, 433
- Ghisellini, G., Celotti, A., Fossati, G., Maraschi, L., & Comastri, A. 1998, *MNRAS*, 301, 451
- Ghisellini, G., Righi, C., Costamante, L., & Tavecchio, F. 2017, *MNRAS*, 469, 255
- Ghisellini, G., & Tavecchio, F. 2008, *MNRAS*, 387, 1669
- Ghisellini, G., Tavecchio, F., & Chiaberge, M. 2005, *A&A*, 432, 401
- Giommi, P., Padovani, P., Polenta, G., Turriziani, S., D'Elia, V., & Piranomonte, S. 2012, *MNRAS*, 420, 2899
- Hagen-Thorn, V. A., Larionova, E. G., Jorstad, S. G., Björnsson, C. I., & Larionov, V. M. 2002, *A&A*, 385, 55
- Hovatta, T., et al. 2014, *MNRAS*, 439, 690
- Igarashi, Y., Takenaka, H., Nakanishi-Ohno, Y., Uemura, M., Ikeda, S., & Okada, M. 2018, *J. Phys. Soc. Jpn.*, 87, 44802
- Ikejiri, Y., et al. 2011, *PASJ*, 63, 639
- Itoh, R., et al. 2016, *ApJ*, 833, 77
- Kaspi, S., Maoz, D., Netzer, H., Peterson, B. M., Vestergaard, M., & Jannuzi, B. T. 2005, *ApJ*, 629, 61
- Kelly, B. C., Bechtold, J., & Siemiginowska, A. 2009, *ApJ*, 698, 895
- Kelly, B. C., Sobolewska, M., & Siemiginowska, A. 2011, *ApJ*, 730, 52
- Kozłowski, S. 2017, *A&A*, 597, A128
- Krishnapuram, B., Carin, L., Figueiredo, M. A. T., & Hartemink, A. J. 2005, *IEEE Trans. Patt. Anal. Mach. Intel.*, 27, 957
- McHardy, I. M., Arévalo, P., Uttley, P., Papadakis, I. E., Summons, D. P., Brinkmann, W., & Page, M. J. 2007, *MNRAS*, 382, 985
- Marscher, A. P., & Jorstad, S. G. 2010, *arXiv:1005.5551*
- Meyer, E. T., Fossati, G., Georganopoulos, M., & Lister, M. L. 2011, *ApJ*, 740, 98
- Narayan, R., & Yi, I. 1995, *ApJ*, 452, 710
- Quataert, E. 2001, in *ASP Conf. Ser.*, 224, *Probing the Physics of Active Galactic Nuclei*, ed. B. M. Peterson et al. (San Francisco: ASP), 71
- Ruan, J. J., et al. 2012, *ApJ*, 760, 51
- Sakimoto, K., et al. 2013, *PASJ*, 65, 35
- Shakura, N. I., & Sunyaev, R. A. 1973, *A&A*, 24, 337
- Shaw, M. S., et al. 2013, *ApJ*, 764, 135
- Sobolewska, M. A., Siemiginowska, A., Kelly, B. C., & Nalewajko, K. 2014, *ApJ*, 786, 143
- Stickel, M., Padovani, P., Urry, C. M., Fried, J. W., & Kuehr, H. 1991, *ApJ*, 374, 431
- Stoeckle, J. T., Morris, S. L., Gioia, I. M., Maccacaro, T., Schild, R., Wolter, A., Fleming, T. A., & Henry, J. P. 1991, *ApJS*, 76, 813
- Uemura, M., et al. 2010, *PASJ*, 62, 69
- Uhlenbeck, G. E., & Ornstein, L. S. 1930, *Phys. Rev.*, 36, 823
- Ulrich, M.-H., Maraschi, L., & Urry, C. M. 1997, *ARA&A*, 35, 445
- Urry, C. M., & Padovani, P. 1995, *PASP*, 107, 803
- Yamada, Y., Uemura, M., Itoh, R., Fukazawa, Y., Ohno, M., & Imazato, F. 2020, *PASJ*, 72, 42